Earthq Eng & Eng Vib (2021) 20: 141-159 **DOI**: https://doi.org/10.1007/s11803-021-2011-1

Seismic response of large-span spatial structures under multi-support and multidimensional excitations including rotational components

Zhang Jie[1†], Li Hongnan[1,2‡] and Li Chao[1§]

1. *State Key Laboratory of Coastal and Offshore Engineering, Faculty of Infrastructure Engineering, Dalian University of Technology, Dalian 116024, China*
2. *School of Civil Engineering, Shenyang Jianzhu University, Shenyang 110168, China*

Abstract: To achieve rational and precise seismic response predictions of large span spatial structures (LSSSs), the inherent non-uniformity and multidimensionality characteristics of earthquake ground motions should be properly taken into consideration. However, due to the limitations of available earthquake stations to record seismic rotational components, the effects of rocking and torsional earthquake components are commonly neglected in the seismic analyses of LSSSs. In this study, a newly developed method to extract the rocking and torsion components at any point along the area of a deployed dense array from the translational earthquake recordings is applied to obtain the rotational seismic inputs for a LSSS. The numerical model of an actual LSSS, the Dalian International Conference Center (DICC), is developed to study the influences of multi-support and multidimensional excitations on the seismic responses of LSSSs. The numerical results reveal that the non-uniformity and multidimensionality of ground motion input can considerably affect the dynamic response of the DICC. The specific degree of influence on the overall and local structural displacements, deformations and forces are comprehensively investigated and discussed.

Keywords: large-span spatial structures; seismic responses; multi-support; multidimensional; rotational components

1 Introduction

Large span spatial structure (LSSS) are a trend in civil engineering today due to their huge open spaces and wide applications in stadiums, high-speed train stations, airport terminals and convention centers, etc. LSSSs are important public facilities, and it is crucial to ensure their safety under earthquake events. Unlike general civil structures, the complexity of LSSS such as shell roof, large suspended parts and complex nodes necessitates a more sophisticated dynamic analysis in the seismic design of such structures.

Previous research in seismology and earthquake damage investigations has revealed that seismic ground motions vary temporally and spatially. The temporal nature of a seismic ground motion means it is a time history, which has been well considered in time history analysis of structures. The spatial nature of seismic ground motion indicates that different points and different directions of the ground move differently during an earthquake, i.e., the non-uniformity and multidimensionality, which have not been thoroughly studied in the dynamic analysis of structures. For a comprehensive understanding of structural seismic responses, the non-uniformity and multidimensionality of input earthquake motions should be well researched, especially for structural styles that are sensitive to the spatial nature of seismic excitations, such as LSSSs.

For structural seismic analyses, uniform input is reasonable when the dimension of the foundation is not comparable with the typical wavelength of earthquake waves. When the foundation size is large (like LSSS), the actual seismic motions at the points on the foundation edge are quite different. The difference can have a huge impact on the response of the structure, such as the change of the initial stress condition caused by the asynchrony of input. A better and realistic understanding of the response of LSSS during an earthquake requires that the excitations vary at different supports (Li *et al*., 2015; Li *et al*., 2018a), i.e., multi-support excitation, instead of uniform excitation. For multidimensionality, the widely accepted input model in seismic design codes is a set of 1:1 translational motions along two horizontal directions or 1:1:0.85 for some special buildings along two horizontal directions and one vertical direction.

Correspondence to: Li Chao, State Key Laboratory of Coastal and Offshore Engineering, Faculty of Infrastructure Engineering, Dalian University of Technology, Dalian 116024, China
E-mail: chaoli@dlut.edu.cn
[†]PhD Candidate; [‡]Professor; [§]Associate Professor

Supported by: National Natural Science Foundation of China under Grant Nos. 51738007, 51808099, the Fundamental Research Funds for the Central Universities under Grant No. DUT20RC(3)005
Received June 30, 2020; **Accepted** October 15, 2020

There are two problems with this model. First, in actual situations, seismic waves incidence the foundation on multi-directions with varying wave shapes, amplitudes and phases, which cannot be included by the simple linear scaling of different translational components. Second, actual ground motions not only consist of three translational components but also of three rotational components around the respective translational directions, which are confirmed to be non-negligible factors in seismic damage of some LSSS and long span bridges (Gupta and Trifunac, 1990; Gupta and Trifunac, 1991; Li *et al*., 1997; Trifunac, 2006; Tian *et al*., 2010; Yang *et al*., 2014; Gu *et al*., 2017). Therefore, in the seismic response analyses of LSSSs, the ground motion inputs should be considered in a multi-support and multi-dimension way (Quan and Li, 2006).

In the consideration of non-uniformity, three effects are typically included: wave passage effect, incoherence effect and local site effect (Li *et al*., 2017; Li *et al*., 2018b). Wave passage effect is caused by the phase difference between the seismic inputs due to the time lag of wave arrival at different structural supports, and it is directly associated with the apparent wave velocity. Incoherence effect is induced by the inhomogeneity of the medium of seismic wave traveling. The complicated reflections and scatterings between different media make the seismic waves incident to the supports, which results in diverse combinations of reflected and scattered waves. Local site effect is due to the inconsistency of local site properties at the supports, which can affect the frequency components of the inputs at different points. There are three popular methods to accomplish multi-support seismic inputs. (1) Take the wave passage effect to represent the entire feature (Lin *et al*., 2013; Yadi *et al*., 2019). However, as the decisive parameter in the wave passage effect, the apparent wave velocity still cannot be precisely obtained (Mu *et al*., 2019). In practice, a vague method for choosing a group of apparent velocities at a wide range (from several hundred to several thousand kilometers per second) is usually applied, which brings large randomness in the analysis results. (2) Use the response spectrum method based on random vibration theory (Alexander, 2008; Soyluk, 2004; Zhao *et al*., 2015), by which the coherence of the dynamic response of different supports between each vibration mode can be considered. However, how to simply and precisely acquire the response spectrum of structures under multi-support and multi-dimension input is still not considered. (3) Apply the spectral representation method to synthesize the spatially varying ground motions at multiple stations for structural seismic analyses (Mirzabozorg *et al*., 2012; Li *et al*., 2018c; Li *et al*., 2020).

In consideration of the multidimensionality of seismic excitation, the translational components of ground motions have been comprehensively studied and applied in engineering applications. Thus, the rotational components of earthquake motions are the focus of this study. Rotational seismology was once doubted and neglected among the majority of seismologists, and with the lag in the development of rotational seismometers, the research in this field had only minor progress in the past few decades (Trifunac, 2009). Until about ten years ago, progress in instrumental science and seismic damage investigations have made rotational seismology an emerging field. The rotational components include two rocking components around two horizontal directions and one torsion component around the vertical direction. Due to the lack of reliable actual rotational ground motion recordings, the research in this field is mostly based on theoretical inference, such as the Geodetic method, synthetic method and focal mechanism-based approach (Lee and Trifunac, 1985; Lee and Trifunac 1987; Spudich *et al*., 1995). However, the comparisons between the inferred rotations and several public rotation motion records reveal that the former ones are one to two orders of magnitude smaller than the latter ones in amplitude. Therefore, the inferred rotations obtained by traditional approaches result in unconvincing multidimensional structural seismic responses.

As discussed above, the key to realize reasonable seismic response analysis of LSSSs under multi-support and multidimensional input is to obtain the precise six-dimensional ground motion time histories at each support. In this study, the translational ground motion recordings from a dense array with a similar size as the foundation of the structure model are applied. A new method based on surface fitting is introduced, by which the rotational components at the supports are obtained. Finally, the time history analysis of an exemplar LSSS under multi-support and multidimensional seismic input is performed. The effects of the rotational components on the seismic responses of LSSS are discussed in detail.

2 Numerical modeling of the exemplar LSSS

The Dalian International Conference Center (DICC, shown in Fig. 1(a)) is selected as the objective LSSSs. The building is located in the north coast of Dalian, and it is 220 m long, 213 m wide and 59 m high. The three-dimensional drawing of the DICC is presented in Figs. 1(b), 1(c) and 1(d). The building area is about 145,000 m^2 and its shape is unique and complex.

In general, the DICC can be divided into four main parts: main body, curved roof, central grand theatre and curtain wall system, as shown in Fig. 2. The main body consists of 16 core tubes as the force transmission system and functional space hanging around the system, as shown in Fig. 3(a). On the top of the core tubes, there are 13 supports to hold the curved roof. On the periphery of main body, the curtain wall system is attached and supported by columns (Fig. 3(b)). The central grand theatre is an independent structure located at the center of the main body. With the exception of the core tubes, which are built with steel reinforced concrete, the rest of the structure is constructed by different specifications

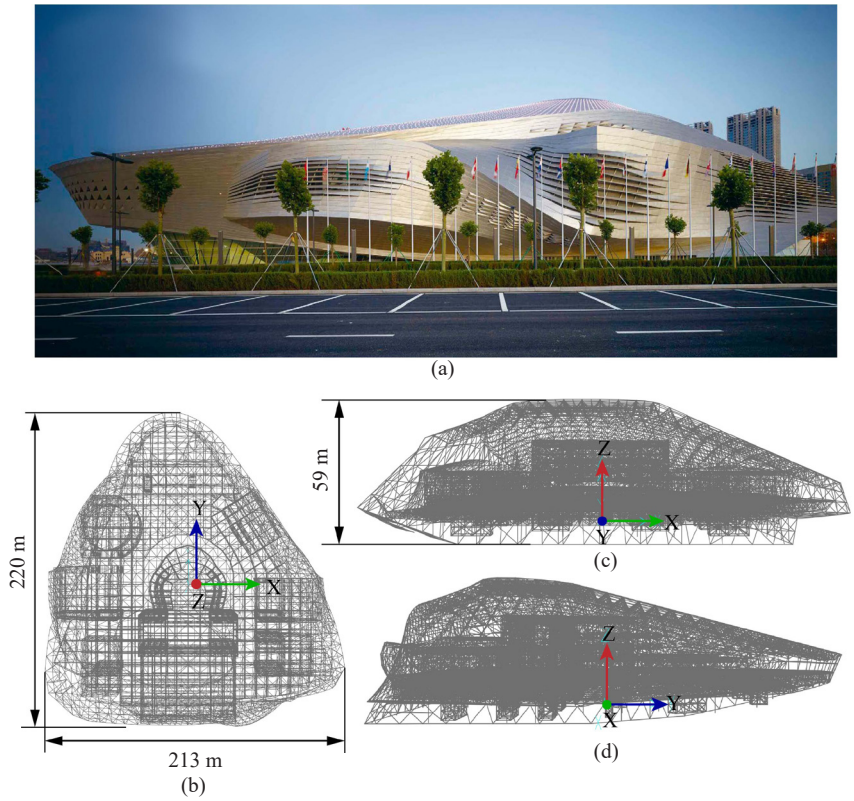

Fig. 1 Actual building and three-dimensional drawing of DICC

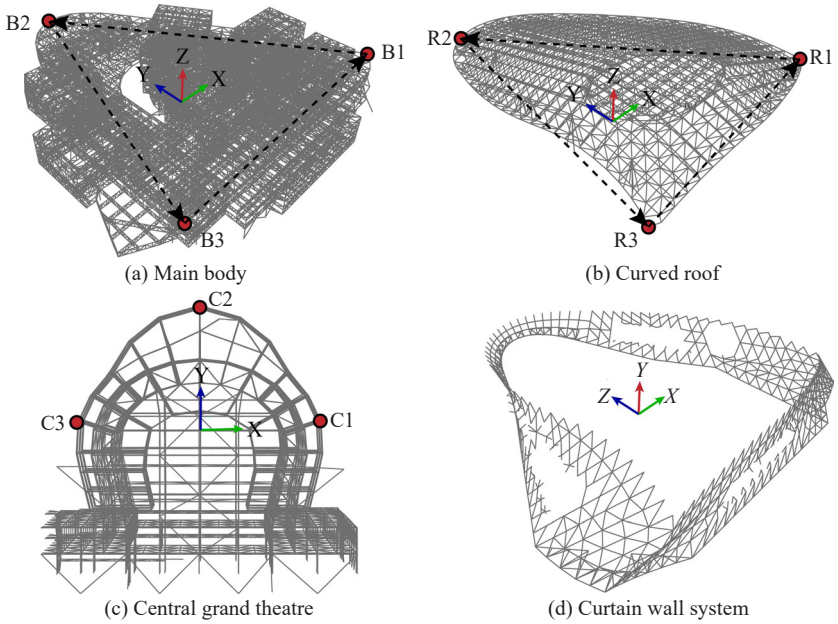

Fig. 2 Four main parts of DICC (The dots in red are the key displacement points and the dashed lines with arrow show the way to calculate average torsions in the result part.)

and types of steel. Due to the structural complexity of the DICC, only a brief introduction is provided here; a more comprehensive introduction of the DICC model can be found in Wang *et al*. (2012). The numerical model of the DICC is developed in the SAP2000 platform. The beams and columns are modeled by a bar element and the walls and floors are modeled by a shell element. A bidirectional oblique twist is formed by the complex curtain wall system. The stress-strain relationships of the materials are present in Fig. 4. There are several unique features of the DICC, including huge weight and uneven distribution of mass (most of the mass is higher than 15.3 m), a large number of core tubes with varying heights, sizes and stiffness and uneven

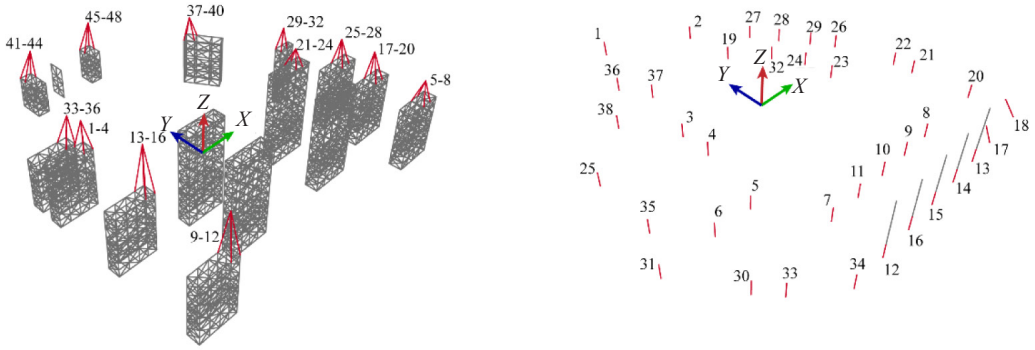

(a) Core tubes and connecting bars (b) Supporting columns

Fig. 3 Core-tube system and supporting system of the DICC (The members highlighted in red are the connecting bars and supporting columns, which are analyzed in result part)

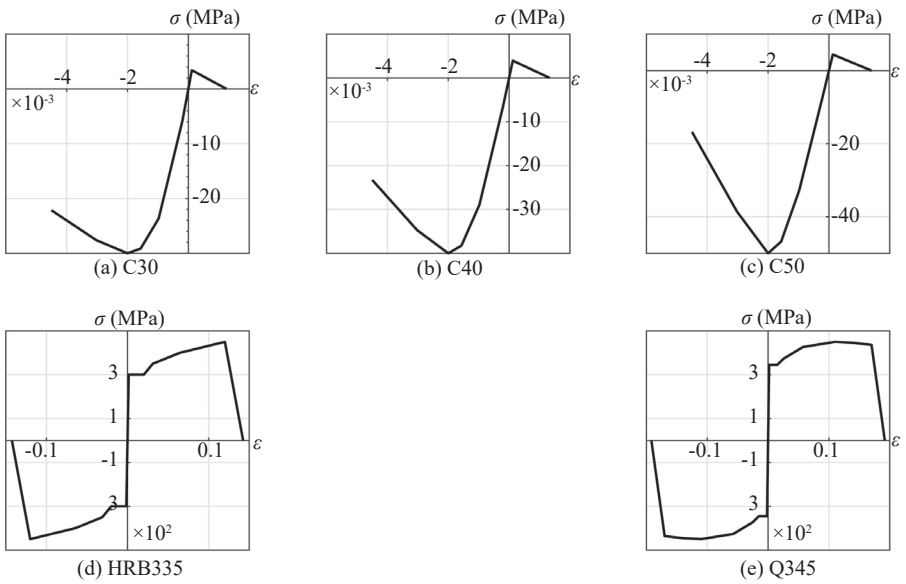

(a) C30 (b) C40 (c) C50

(d) HRB335 (e) Q345

Fig. 4 Strain-stress curves of the materials used in the numerical model

distribution among the foundation, and the large distance between the tubes and large suspended parts around the periphery, etc. All these features are harmful for seismic safety of the DICC; thereby, the multi-support and multidimensional ground motion inputs are required to comprehensively assess the structural seismic responses.

3 Surface fitting method (SFM)

3.1 Introduction of SFM

A primary method to obtain rotational ground motion is from the translational recordings of seismic dense arrays, such as the widely accepted geodetic method. In this research, a new method to extract rotational components from a dense array proposed by the authors is applied to calculate the corresponding rotational ground motion inputs (Zhang *et al*., 2020a, 2020b). The following is a brief introduction of this method.

The ground surface deforms as a seismic wave passes through it. The shape of the surface is the joint effect of all the translational and rotational components of ground motion. If the ground shape at a time instant during an earthquake can be determined or approximated, then the corresponding rotational components at that instant can be obtained. Recordings of dense arrays provide a relatively intense displacement field which can be used to simulate the surface shape. The rotations can be described by the curvature of the curves along the surface. In (Zhang *et al*., 2020a), it is revealed that a paraboloid is a reasonable description of the surface shape of the array used in this research. The surface fitting method used in this study is divided into two parts: rocking calculation and torsion calculation, and they are illustrated in Fig. 5. The detailed procedures of the rotational components calculation are as follows:

(1) As shown in Fig. 5(a), choose the center of an array as the origin of an *XYZ* coordinate system. At time instant t_j, the positions of the observed point among the array are fitted to a paraboloid F by multi-linear regression. The surface is described by Eq. (1).

$$Z_i^P(X_i, Y_i) = aX_i^2 + bY_i^2 + cX_iY_i + dX_i + eY_i + f_i \quad (1)$$

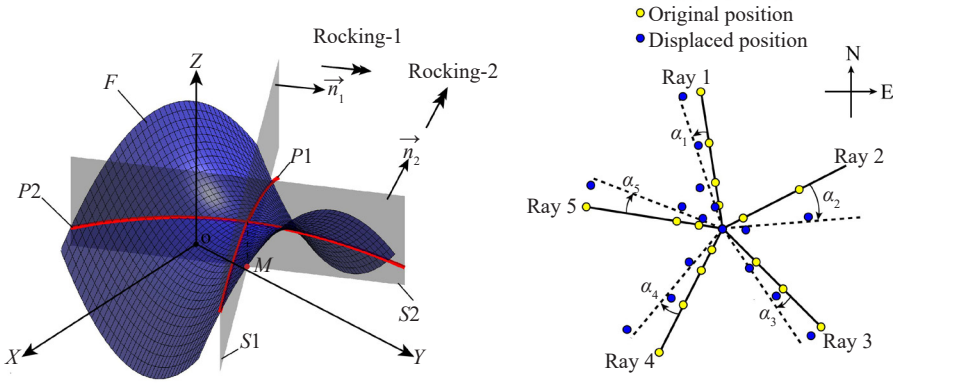

(a) Illustration of rocking components calculation (b) Illustration of torsion component calculation

Fig. 5 Illustration of surface fitting method

in which a,b,c,d,e are the parameters determined by multi-linear regression. $\left(X_i,Y_i,Z_i^P\right)$ are the points on the fitted paraboloid.

(2) Randomly select a point $M(x_m,y_m)$ on the array surface, define two orthogonal vertical planes $S1$ and $S2$, both passing through $M(x_m,y_m)$, with their normal vector $\vec{n}_1,\vec{n}_2$, as shown in Eq. (2)

$$\begin{aligned} Y_1(X) &= kX+m \\ Y_2(X) &= (-1/k)X+n \end{aligned} \tag{2}$$

in which

$$\begin{aligned} m &= -kx_m+y_m \\ n &= x_m/k+y_m \end{aligned}$$

where k is the slope of the normal vector of plane $S1$, and (-1/k) is that of $S2$.

By solving the equation of the fitted paraboloid and the vertical planes, the intersecting curves between F and $S1$, $S2$ can be represented by Eq. (3). Both curves are parabolas.

$$\begin{aligned} P1:&\quad Z_1(X)=A_1X^2+B_1X+C_1 \\ P2:&\quad Z_2(X)=A_2X^2+B_2X+C_2 \end{aligned} \tag{3}$$

in which

$$\begin{cases} A_1=a+bk^2+ck \\ B_1=2bkm+cm+d+ek \\ C_1=bm^2+em+f \end{cases} \quad \begin{cases} A_2=a+b/k^2-c/k \\ B_2=-2bn/k+cn+d-e/k \\ C_2=bn^2+dn+f \end{cases}$$

Then the curvature of $P1$ and $P2$ can be computed by

$$\begin{aligned} \kappa_1 &= \frac{\left|Z_1''(X)\right|}{\left(1+\left[Z_1''(X)\right]^2\right)^{3/2}} = \frac{\left|2A_1\right|}{\left(1+\left[2A_1X+B_1\right]^2\right)^{3/2}} \\ \kappa_2 &= \frac{\left|Z_2''(X)\right|}{\left(1+\left[Z_2''(X)\right]^2\right)^{3/2}} = \frac{\left|2A_2\right|}{\left(1+\left[2A_2X+B_2\right]^2\right)^{3/2}} \end{aligned} \tag{4}$$

The curvature of $P1$ and $P2$ changes with the position on the parabola; here, the average curvatures among the range of the array are selected as their extent of bending, as in Eq. (5).

$$\overline{\kappa}_1=\frac{1}{N}\sum_{j=1}^{N}\kappa_{1,j},\ \overline{\kappa}_2=\frac{1}{N}\sum_{j=1}^{N}\kappa_{2,j} \tag{5}$$

in which N is the number of the points selected along $P1$ and $P2$.

According to the definition of average curvature shown in Eq. (6), when $\overline{\kappa}$ and Δs are known, the induced angle of the tangent $\Delta\alpha$ at a point on the curve can be calculated by Eq. (7), which can be taken as the rocking of the surface around the direction perpendicular to the curve.

$$\overline{\kappa}=\left|\frac{\Delta\alpha}{\Delta s}\right| \tag{6}$$

$$\Delta\alpha=\overline{\kappa}\cdot\Delta s \tag{7}$$

in which $\overline{\kappa}$ is the average curvature, $\Delta\alpha$ is the included angle of the tangent at a point on the curve and Δs is the length of the curve.

Since the description of $P1$ and $P2$ is analytical, their length can be precisely calculated; called L_1 and L_2 for $P1$ and $P2$, respectively. As shown in Fig. 5(a), the rocking angle around the normal vector of $P1$ and $P2$

can be determined by Eq. (8).

$$\begin{aligned} \text{Rocking}_1 &= \bar{\kappa}_1 L_1 \\ \text{Rocking}_2 &= \bar{\kappa}_2 L_2 \end{aligned} \tag{8}$$

Through the above deduction, a pair of rocking components around two orthogonal directions at any point among the array surface can be determined.

For the torsion component, the idea is to calculate the average of some segments formed by the points among the array before and during earthquake. One method is to form a group of segments by connecting any two stations, then average their torsion angles. The other is to calculate the mean torsion of the rays composed by the stations along those directions from the center of the array. The analysis results show that the torsion components computed from the two methods are almost identical. For simplicity, the second method is selected herein, which is illustrated in Fig. 5(b). The torsion angle at any time instant then can be determined by Eq. (9).

$$\text{Torsion} = \frac{1}{5}\sum_{i=1}^{5}\alpha_i \tag{9}$$

In this section, a brief introduction on the surface fitting method to obtain the rotational ground motions is provided. Note that the rocking components are not only related to the position of the studied point but also depend on the directions of the two defined vertical planes. In this study, the recorded translations are along the *X*, *Y* and *Z* directions, so in rocking computation, the directions of *S*1 and *S*2 in Fig. 5(a) coincide with the *X* and *Y* axes. Moreover, the principles for rocking computation and torsion computation are different. The former one is a second order curved surface approximation and the latter one is a one order approximation (the ground is treated as a whole rigid plane rotating around *Z* axis), which means the torsion component is identical at any point on the surface.

3.2 Validation of SFM

The validation of SFM requires comparison with directly recorded time histories of rotational components. In 2014, there was a program called SINAPS@ conducted on Cephalonia Island, Greece. In this program, a dense array consisting of 21 translational seismometers and one rotational seismometer at the center were deployed and a dataset with both translational and rotational recordings for each earthquake was obtained (Imtiaz *et al*., 2018). SFM was applied to the translational displacement field of this dataset to derive the rotational components at the center and compared with the rotational seismometer recordings at the same point. Good agreement between the SFM derived rocking and recorded rocking were observed. Here, two typical events are presented in Fig. 6(a), with an Ormsby filter from 0.5–1 Hz to 20–25 Hz. As illustrated, the SFM derived time histories of the rocking components and the actual recordings are close to each other, especially around the peak rocking for both events. The large discrepancy among the amplitude of rotational components can be explained by the difference in the essence for rocking and torsion component calculation schemes, shown in Fig. 5, in which rocking computation is based on a second order approximation of the surface while that of torsion computation is only one order approximation. For a better comparison between the wave form, the time histories are normalized by their peak values, as shown in Fig. 6(b). The wave form of all the rotational components of SFM are alike with actual recordings.

If the time histories are filtered to a more common frequency range for use in civil engineering, such as 0.5–1 Hz to 5–6 Hz, the coincidence becomes even better, as shown in Fig. 7. SFM obtained rocking components from Event #1 are almost identical to the actual rocking recordings. This phenomenon implies that SFM can produce rocking components with high reliability for civil engineering purposes, such as seismic response analysis. A more comprehensive study on the rationality and advances in SFM are provided in Zhang *et al*. (2020b).

4 Data of translational seismic recordings

The translational seismic motions used in this study are recorded by the Array S in Program NERA. Array S is installed in a basin near the town of Argostoli, Cephalonia Island, Greece (Imtiaz *et al*., 2018). As shown in Fig. 8, Array S consists of 21 three-axis translational seismometers, which are evenly distributed on the circles with radius of 0, 5 m, 15 m, 40 m and 80 m, forming five rays originating from the central station. A series of earthquake events were recorded and two principals were followed in event selection: (1) to achieve prominent seismic structural responses, choose earthquakes with strong signals (i.e., large magnitudes); (2) for the diversity of analysis, choose events with significant differences in basic earthquake characteristics. Finally, a far-field earthquake with M_L=4.6, event #21 and a near-field earthquake with M_L=3.5, event #36, are chosen as the translational seismic input herein, with the basic information listed in Table 1.

5 Multi-support and multidimensional inputs

The DICC is basically supported by the 16 core tubes, from which the ground motions transmit into the structure. The diameter of Array S is 160 m and it is close to the size of the foundation of the DICC. Fig. 9 illustrates the DICC numerical model in Array S with the angles adjusted. All 141 foundation nodes are divided into five groups by keeping the closeness of the nodes and the large distance between groups, namely G1-G5

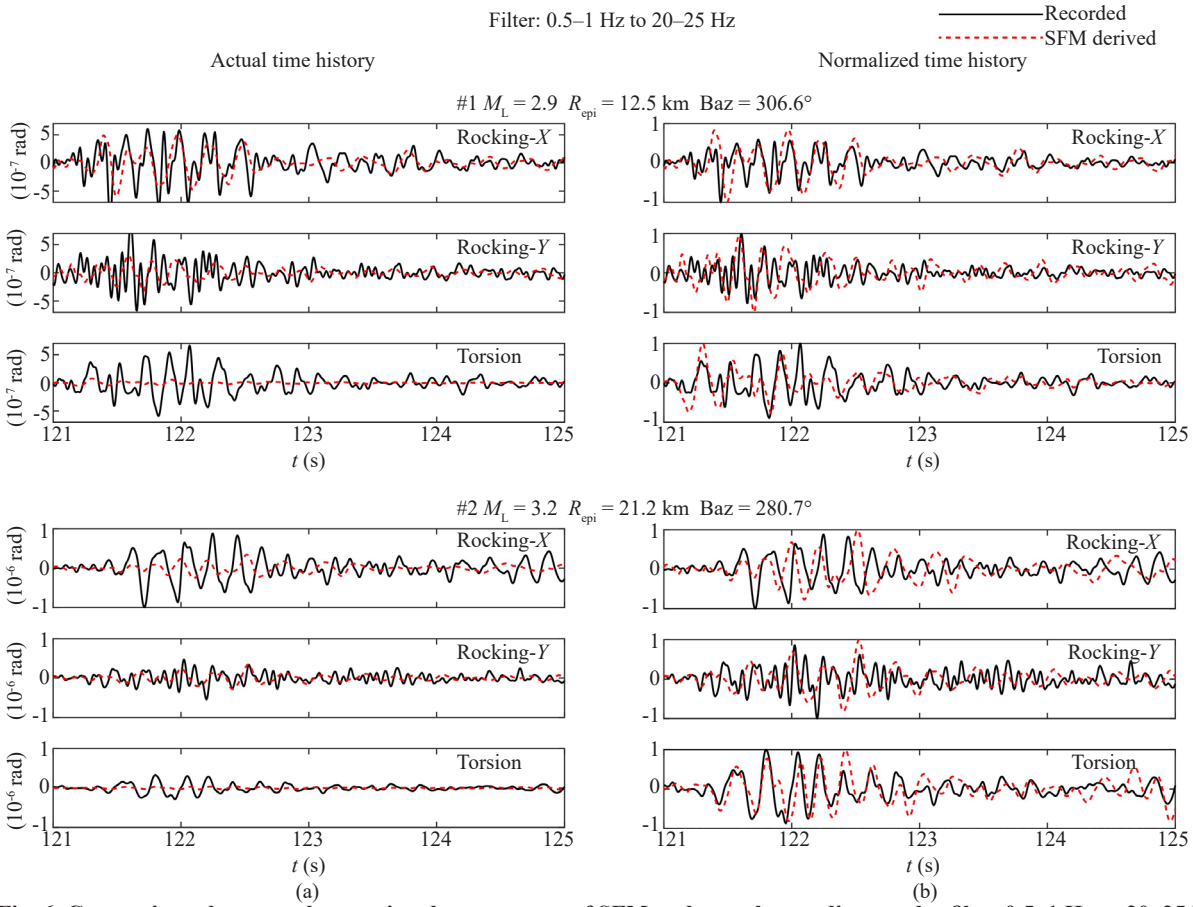

Fig. 6 Comparisons between the rotational components of SFM and actual recordings under filter 0.5–1 Hz to 20–25 Hz

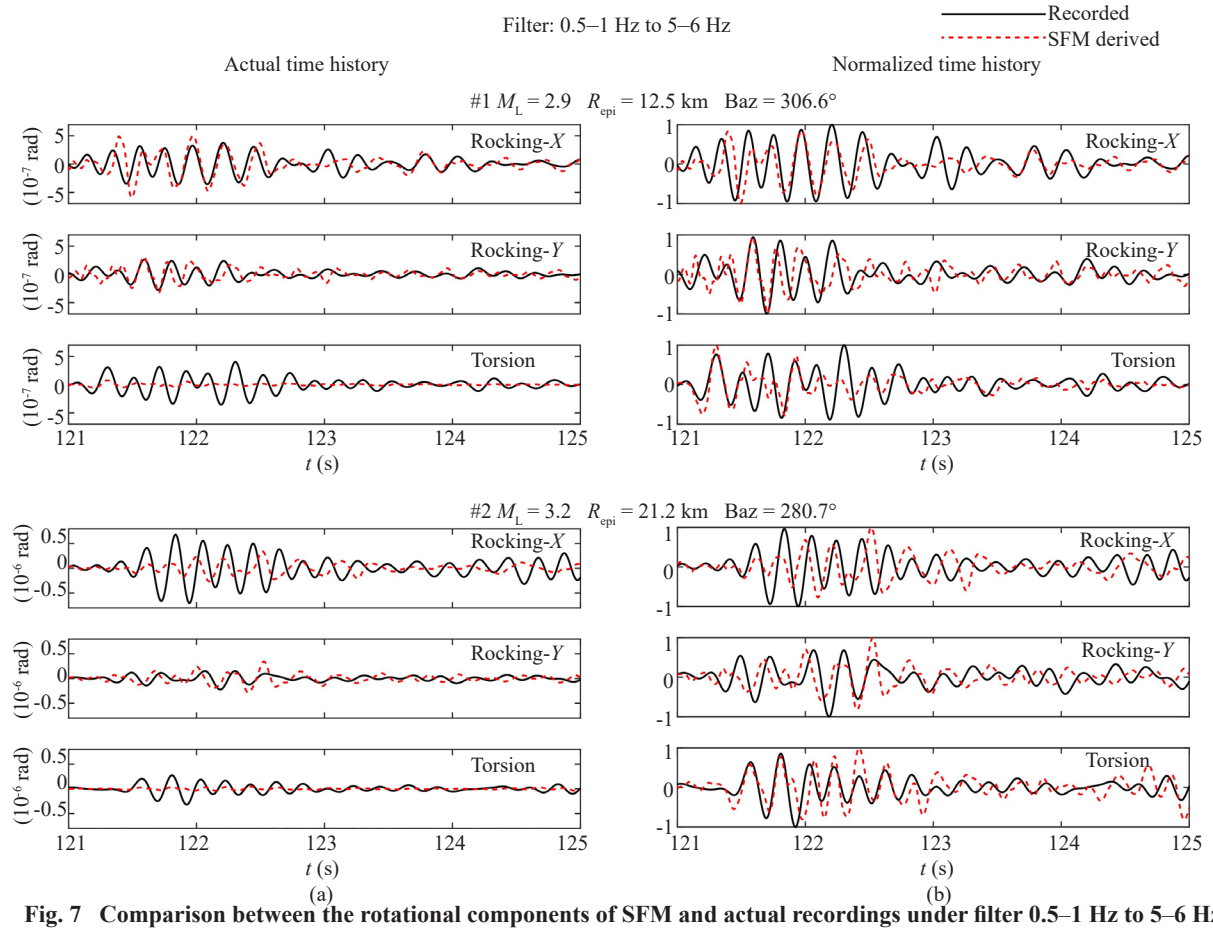

Fig. 7 Comparison between the rotational components of SFM and actual recordings under filter 0.5–1 Hz to 5–6 Hz

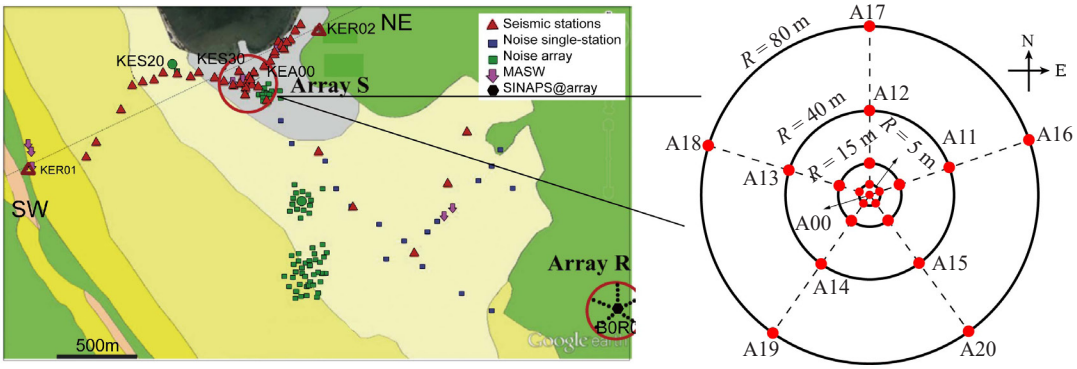

Fig. 8 Information of Array S (Imtiaz *et al*., 2018)

Table 1 Basic information of the selected earthquake events

Event	M_L	Depth (km)	Epicentral distance (km)	PGA (g)
#21	4.6	19	119.3	0.00194
#36	3.6	18.5	3.1	0.0177

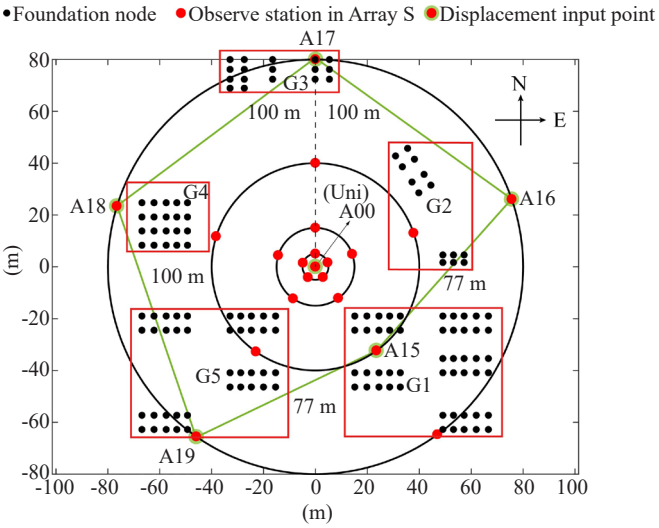

Fig. 9 Foundation nodes groups and input point representation

in the figure. For each group of foundation nodes, a station is chosen as a representation of the seismic input point. Here, the stations A15–A19 are chosen for G1–G5, respectively (A20 is not selected for G1 due to its dysfunction during #21 and #36). As the control group, a uniform input case is needed in the analysis. The ground motions at A00, i.e., the central station, are chosen as the uniform inputs for all the foundation nodes in the uniform excitation case.

The mainstream approaches for multi-support input include the large-mass method, large stiffness method and displacement input method (Luo *et al*., 2015). In this research, the displacement input method is selected, which can be straightforwardly performed in SAP2000 (Luo *et al*., 2015). By applying the surface fitting method at the selected seismic input points, the rocking and torsional components are computed. Along with the translational recordings, the six-dimensional ground motion time histories at multiple supports are obtained for events #21 and #36, as shown in Figs. 10 and 11. For a better understanding of the input displacement time histories, the response spectra of the displacements and accelerations are shown in Figs. 12 and 13, respectively. The major responses are concentrated on structures with natural frequencies of 1 Hz–8 Hz for the acceleration response spectra and 1 Hz–4 Hz for the displacement response spectra.

The actual soil site of the DICC belongs to Category II, which is a seismically unfavorable site with predominant periods of 0.137 s, 0.135 s and 0.147 s on the E-W, S-N and T-D directions, respectively. Based on the Code for seismic design of buildings (GB 50011-2010, 2010) and the Seismic ground motion parameter zonation map of China (GB 18306-2015, 2015), the seismic fortification intensity of the Dalian district is 7 degree and the design basic acceleration of ground motion is 0.1 g. To study the seismic performance of the DICC under major earthquakes in the Dalian district, the peak ground accelerations (PGAs) of events #21 and #36 are scaled to 0.22 g in the time history analysis. Moreover, the direct integration method on the SAP2000 platform is employed in the numerical simulation. Four load cases were selected for each earthquake event, including uniform translational motion input (denoted by “Uni”), uniform translational motion and three rotational motion input (“Uni+3R”), multi-support three translational motion input (“Multi”), multi-support translational motion and three rotational motion input (“Multi+3R”). Note that the rotational seismic inputs in Case “Uni+3R” are different from those in Case “Multi+3R”. In the former case, the rotational components computed at the central station (A00) are employed; while the rotation components obtained at multiple input points (A15–A19) are used in the latter case.

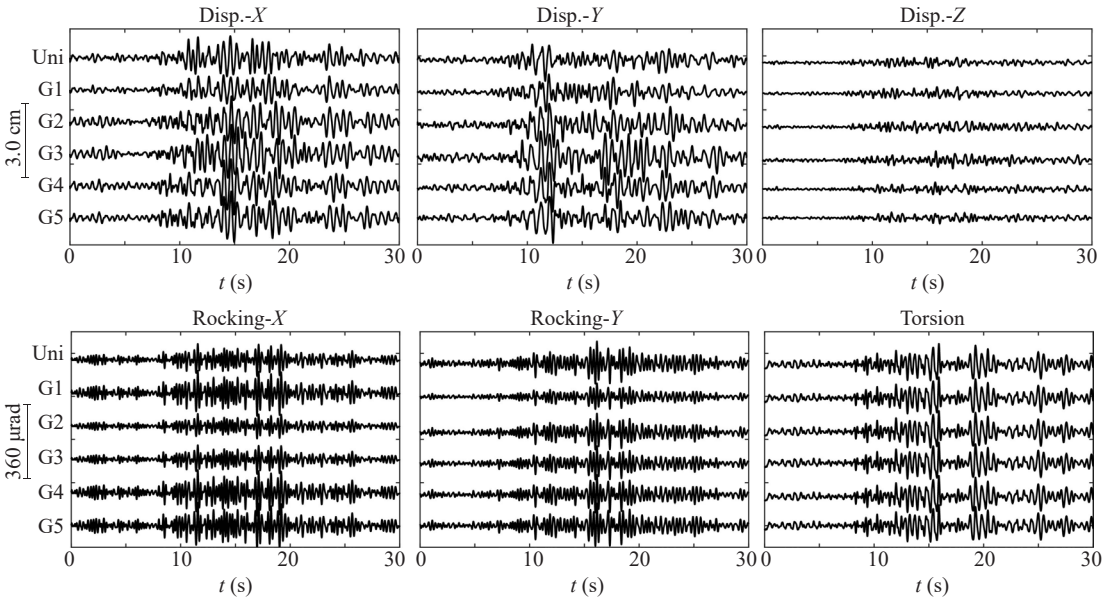

Fig. 10 Multidimensional ground motion time histories for different supports of event #21

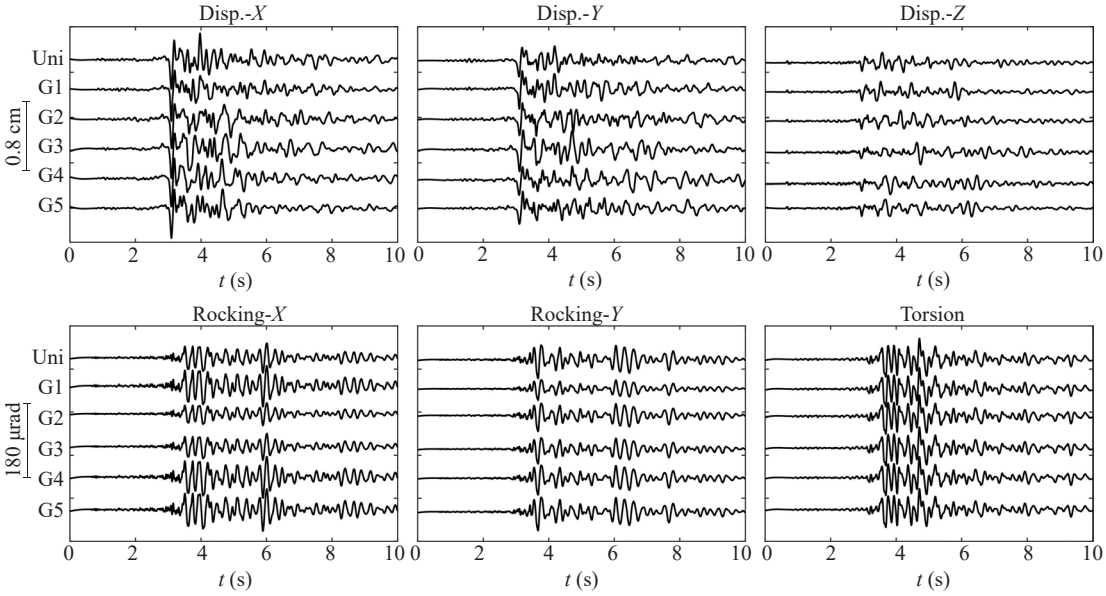

Fig. 11 Multidimensional ground motion time histories for different supports of event #36

6 Results and discussion

The seismic performance of the exemplar LSSS is investigated from two aspects: overall response and local response. Overall response includes the displacements at key points and the average torsion response of the main body and curved roof, as well as the base reaction time histories. Local response includes the response of the connecting rod between main body and roof, and the response of the supporting columns at the foundation. Modal analysis is conducted first. As shown in Table 2, the natural frequency of DICC is 1.7252 Hz. The principal mode in the *X* direction is Mode 7 with a frequency of 2.6185 Hz, as shown in Fig. 14(a). The principal mode in the *Y* direction is Mode 1 with a frequency of 2.6185 Hz, as shown in Fig. 14(b). The principal mode in the *Z* direction is Mode 14 with a frequency of 4.2753 Hz, as shown in Fig. 14(c). The principal torsion mode is Mode 5 with a frequency of 2.3601 Hz, as shown in Fig. 14(d).

6.1 Overall response

6.1.1 Peak displacements of key points

The key points for different parts of the DICC model are labeled with red dots in Fig. 2. The peak displacement responses of these key points under different cases are shown in Fig. 15. Generally, the non-uniformity of seismic input significantly affects the response, while

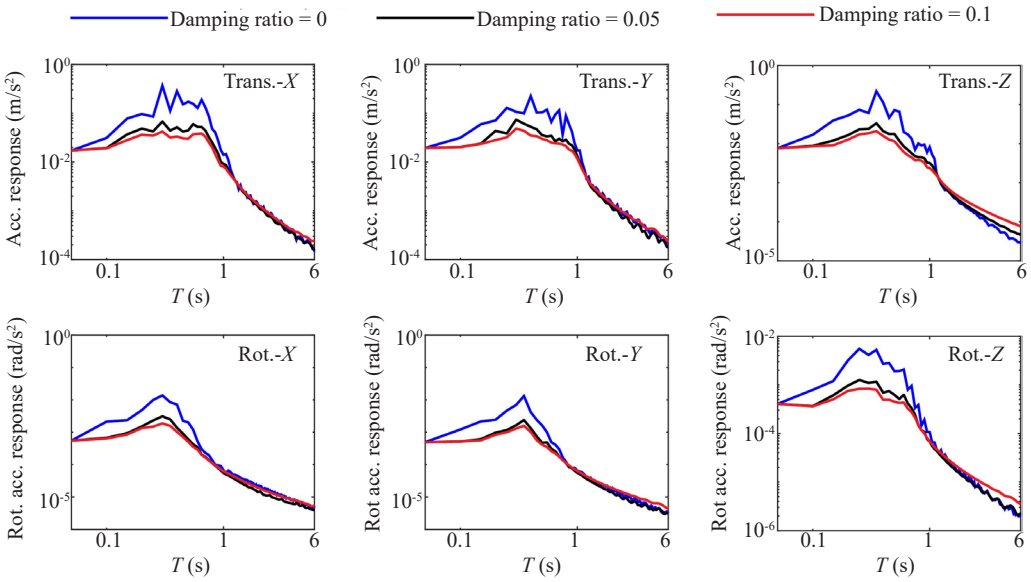

(a) Translational and rotational acceleration response spectra for Event #21

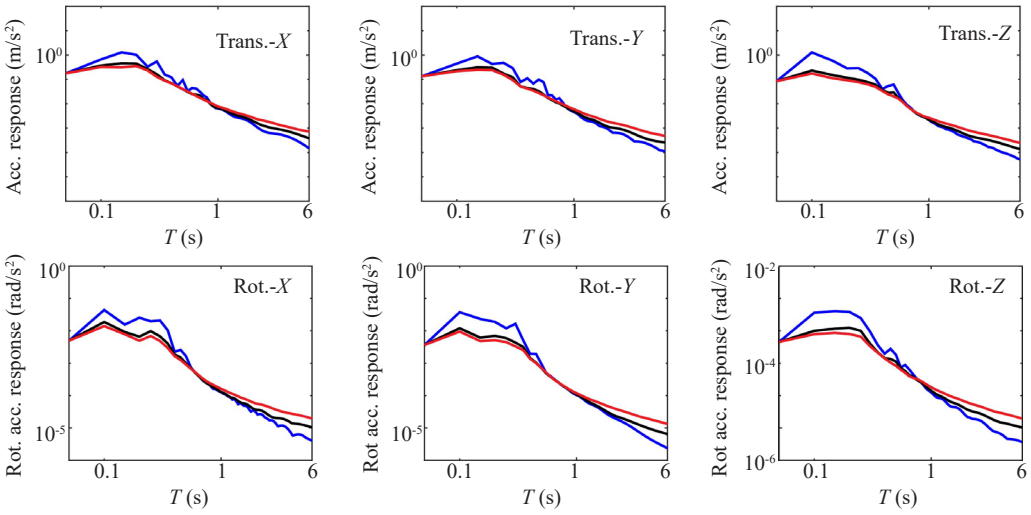

(b) Translational and rotational acceleration response spectra for Event #36

Fig. 12 Translational and rotational acceleration response spectra of two events at A00

Table 2 Modes and frequencies

Mode	Frequency (Hz)	Mode deformation	Mode	Frequency (Hz)	Mode deformation
1	1.7252	*Y*	5	2.3601	*RZ*
2	1.8463	Local vibration	7	2.6185	*X*
3	1.9983	Local vibration	14	4.2753	*Z*
4	2.2809	Local vibration	–	–	–

the multidimensionality of input does not result in an influence comparable with that of the non-uniformity. There are three features of influence from non-uniformity and multidimensionality, as follows. (1) The non-uniformity mostly increases the displacement with an average increase of about 15% and the largest rise is the torsion angle of B2 in the main body under event #36, about 320%. Also, some decreases occur when the average decrease was less than 5% and the largest was about 130% of the vertical displacement of R3 in the curved roof. (2) Under uniform seismic input, the rotational components hardly affect the displacement response; while under multi-support inputs, the rotational components notably increase the displacement.

6.1.2 Average torsion responses

The torsion responses of the main body and curved roof are selected to study the change of the deformation pattern under different load cases. For a better

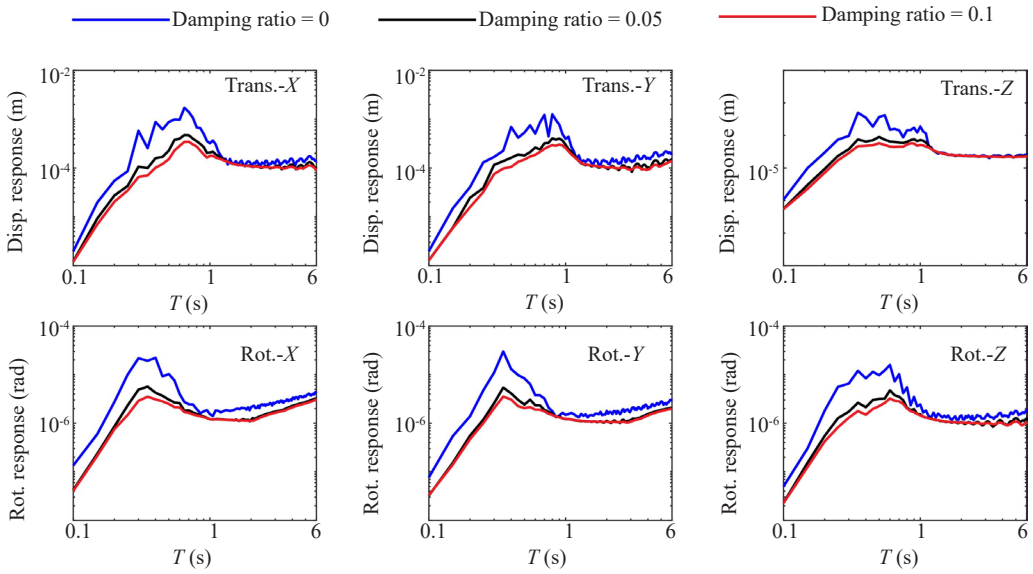

(a) Translational and rotational displacement response spectra for Event #21

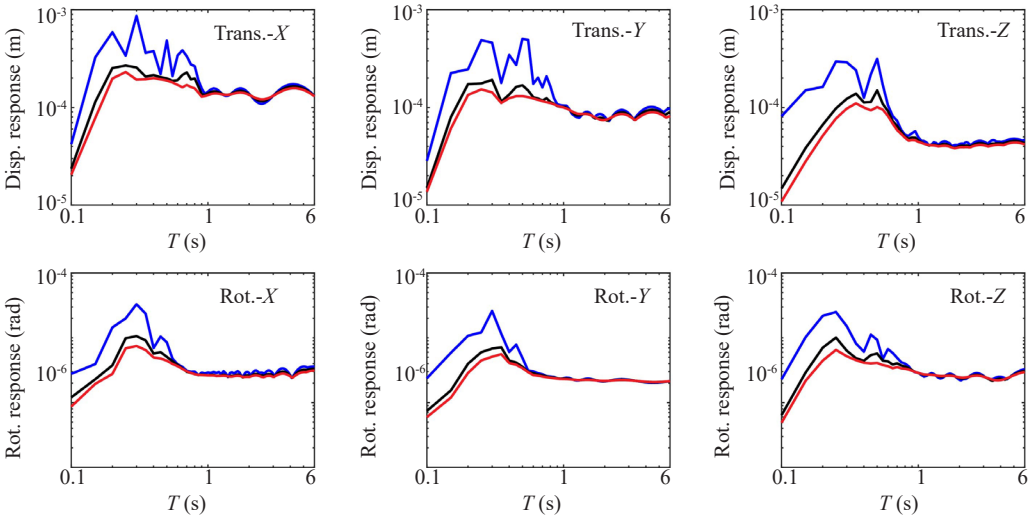

(b) Translational and rotational displacement response spectra for Event #36

Fig. 13 Translational and rotational displacement response spectra of two events at A00

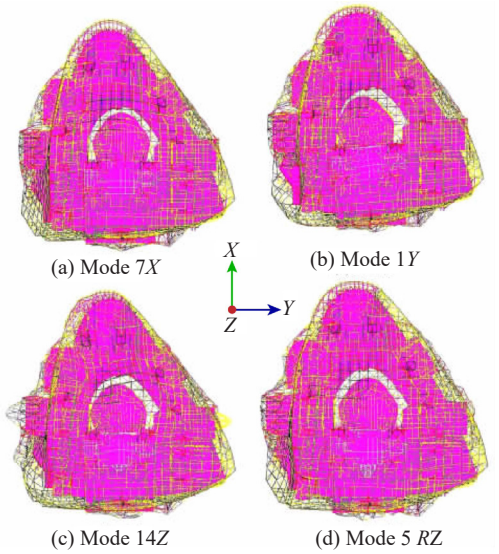

Fig. 14 Principal modes on *X*, *Y* and *Z* and principal torsion mode

representation of the overall reaction, the averaged torsion is studied instead of the torsion at a local point. The main body is used as an example to illustrate how the average torsion is calculated. As shown in Fig. 2(a), the positions before and during the earthquake of the three counterclockwise key points selected on the periphery of main body B1, B2 and B3 are (x_1, y_1), (x_2, y_2) and (x_3, y_3), $(x_1 + \Delta x_1, y_1 + \Delta y_1)$, $(x_2 + \Delta x_2, y_2 + \Delta y_2)$ and $(x_3 + \Delta x_3, y_3 + \Delta y_3)$, respectively. Then, the rotation of segment B1-B2 is:

$$\varphi_{1\to 2} = \tan^{-1}\left(\frac{\left(\left(y_2 + \Delta y_2\right)\right) - \left(y_1 + \Delta y_1\right)}{\left(\left(x_2 + \Delta x_2\right)\right) - \left(x_1 + \Delta x_1\right)}\right) - \tan^{-1}\left(\frac{y_2 - y_1}{x_2 - x_1}\right) \tag{10}$$

In the same way, the rotations of B2-B3 and B3-B1, i.e., $\varphi_{2\to 3}$ and $\varphi_{3\to 1}$, can be calculated. The average value of the three rotations is the average torsion of the

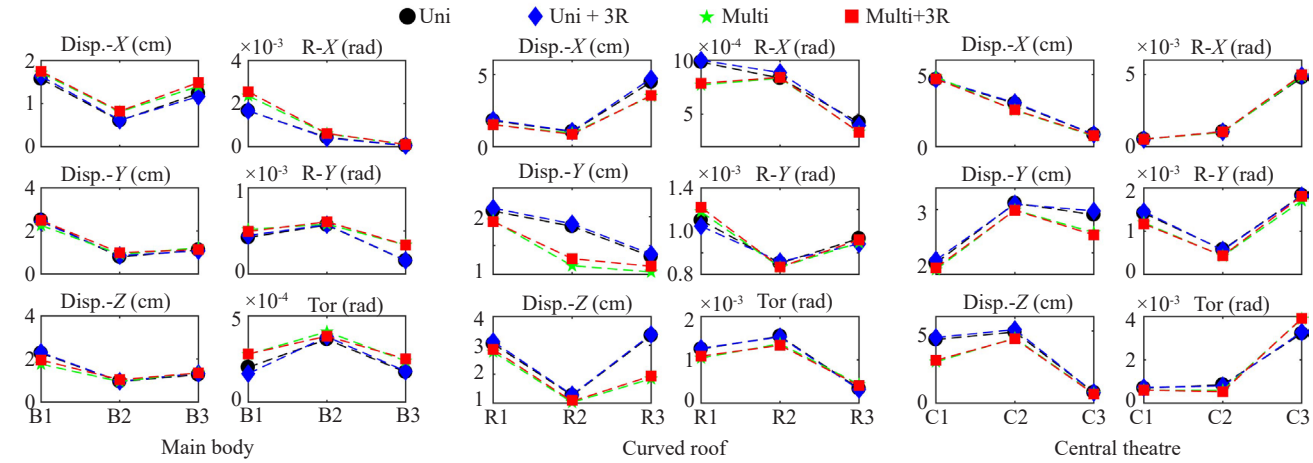

(a) Peak displacement of the key points for different parts for #21

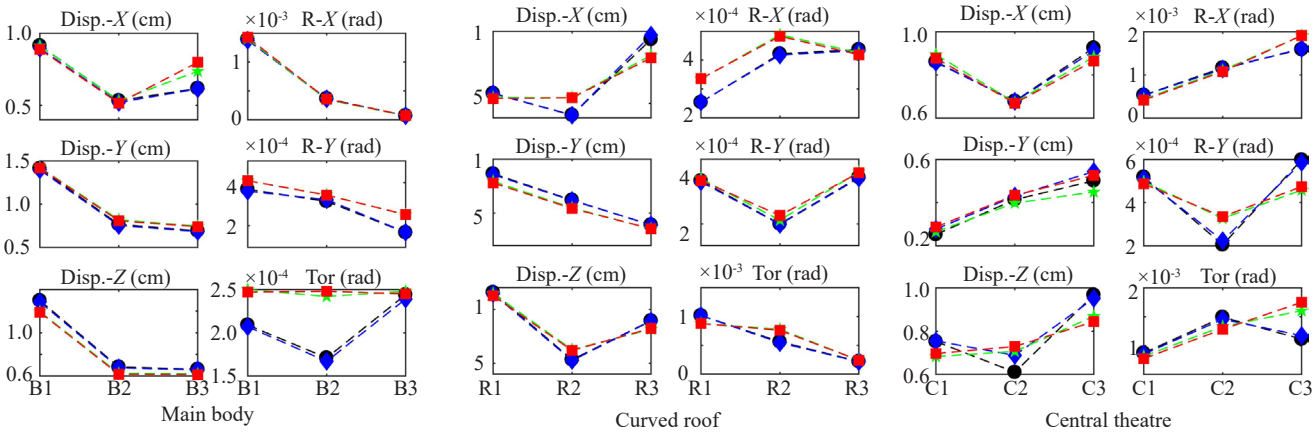

(b) Peak displacement of the key points for different parts for #36

Fig. 15 Peak displacements at key points under different load cases

main body, as shown in Eq. (11).

$$\overline{\varphi}_{\mathrm{B}}=\frac{1}{3}\left(\varphi_{1\to 2}+\varphi_{2\to 3}+\varphi_{3\to 1}\right) \tag{11}$$

For the curved roof, the average torsion $\overline{\varphi}_{\mathrm{R}}$ can be computed with the same procedure, then the relative torsion between the two parts can be calculated by $\overline{\varphi}=\overline{\varphi}_{\mathrm{B}}-\overline{\varphi}_{\mathrm{R}}$. Figure 16 shows plots of the time histories of average torsion and relative torsion for the main body and curved roof under events #21 and #36. For both earthquakes, the multi-support input significantly increases $\overline{\varphi}_{\mathrm{B}}$, $\overline{\varphi}_{\mathrm{R}}$ and $\overline{\varphi}$. The torsion of the main body is much smaller than that of the roof due to the high torsional stiffness provided by the steel reinforced concrete core tubes similar to the situation with peak displacements of key points, the rotational components hardly have an influence on the torsion response for the uniform input cases. Table 3 summarizes the peak torsions of different cases and their comparison with Case Uni. For #21, the multi case increases $\overline{\varphi}_{\mathrm{B}}$, $\overline{\varphi}_{\mathrm{R}}$ and $\overline{\varphi}$, with 20.83%, 83.34% and 16.14%, respectively. When the rotational components are considered, the influences on $\overline{\varphi}_{\mathrm{B}}$ and $\overline{\varphi}$ are reduced to 12.57% and 9.77%. The rotations here positively contribute to the seismic resistance of the structure. However, this phenomenon does not occur in event #36 with similar influence of Multi and Multi+3R cases, which both strongly rise $\overline{\varphi}_{\mathrm{B}}$, $\overline{\varphi}_{\mathrm{R}}$ and $\overline{\varphi}$ with about 52%, 25% and 82%. Meanwhile, the frequency analyses of $\overline{\varphi}$ for #21 and #36 shows that under multi-support input, the relative average torsion has more high frequency content than that under uniform input. It is revealed that non-uniformity and multidimensionality can induce torsion motions with higher frequency and larger amplitude between the main body and the curved roof. The response coordination between the two crucial parts and the stability of the roof are under more serious challenges when the input is non-uniform and multidimensional.

6.1.3 Base reaction

The base reaction time histories and the peak reactions of four load cases are compared. Figures 17 and 18 show the results for #21 and #36 and Table 4 presents a summary of the peak reactions. Compared with the impact brought by the non-uniformity of input,

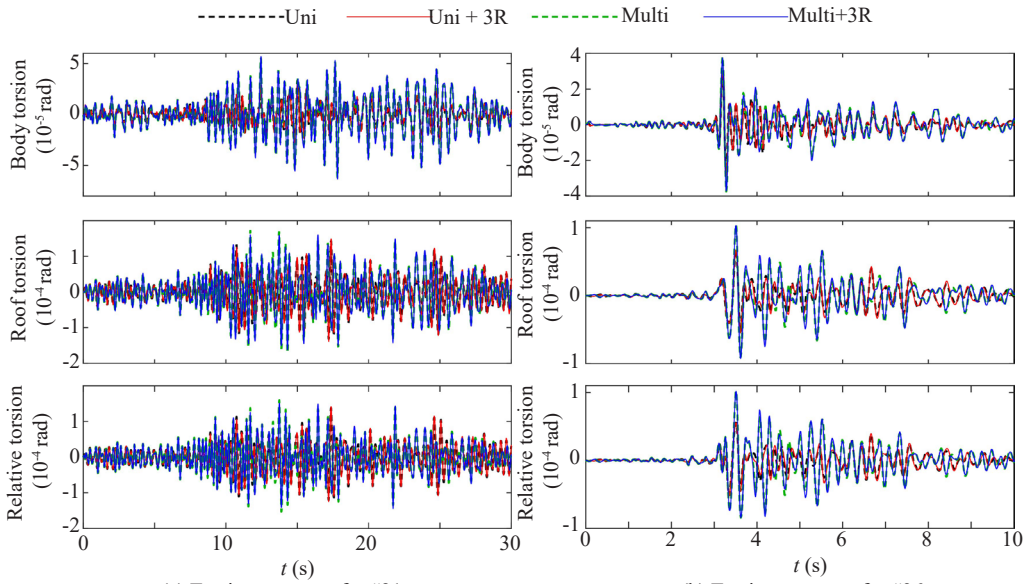

(a) Torsion response for #21 (b) Torsion response for #36

Fig. 16 Average torsion of main body and roof and relative torsion for #21 and #36

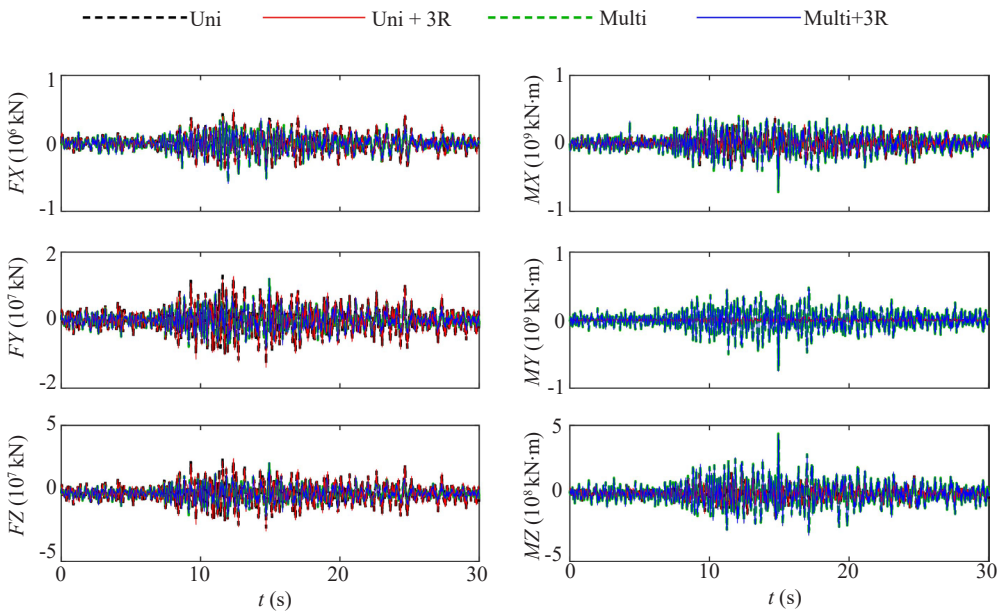

Fig. 17 Time histories of base reactions for #21

Table 3 Peak $\overline{\varphi}_B$, $\overline{\varphi}_R$ and $\overline{\varphi}$ under four load cases

Events	Cases	$\overline{\varphi}_R$ (μrad)	$\overline{\varphi}_B$ (μrad)	$\overline{\varphi}$ (μrad)	$\Delta\overline{\varphi}_R$	$\Delta\overline{\varphi}_B$	$\Delta\overline{\varphi}$
#21	Uni	14.36	3.37	13.78	--	--	--
	Uni+3R	14.87	3.24	14.17	3.49%	-3.88%	2.83%
	Multi	17.36	6.17	16.00	20.83%	83.34%	16.14%
	Multi+3R	16.17	6.34	15.12	12.57%	88.26%	9.77%
#36	Uni	6.79	3.01	5.60	--	--	--
	Uni+3R	6.72	2.97	5.52	-1.03%	-1.33%	-1.43%
	Multi	10.30	3.81	10.18	51.69%	26.58%	81.84%
	Multi+3R	10.30	3.76	10.17	51.69%	24.92%	81.59%

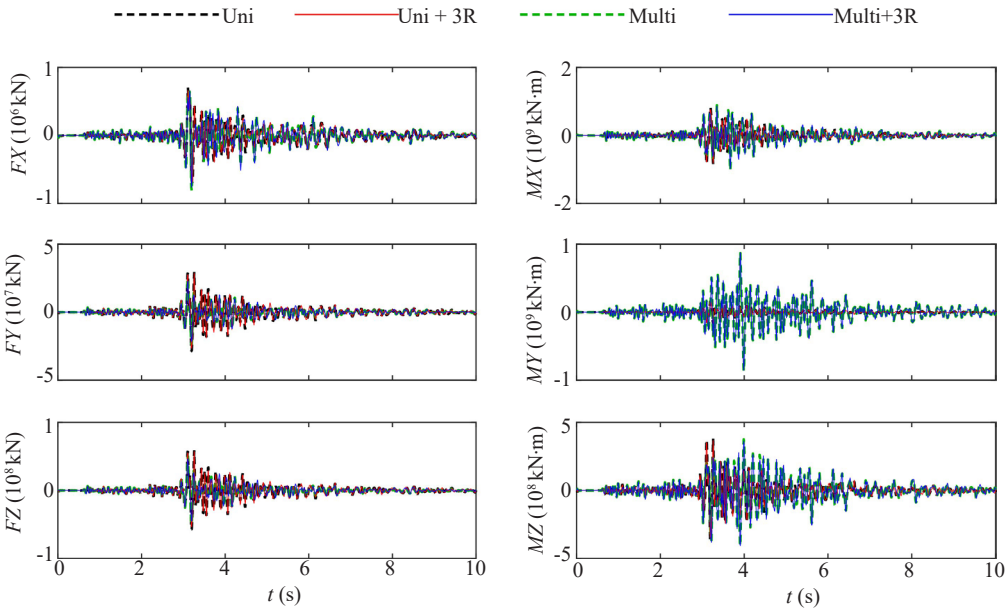

Fig. 18 Time histories of base reactions for #36

Table 4 Peak base reactions for #21 and #36 under four load cases

		FX (×10⁶ kN)	*FY* (×10⁶ kN)	*FZ* (×10⁶ kN)	Δ*FX*	Δ*FY*	Δ*FZ*
#21	Uni	4.60	13.31	26.58	--	--	--
	Uni+3R	5.03	13.95	27.76	9.28%	4.77%	4.44%
	Multi	5.71	12.86	23.75	24.09%	-3.42%	-10.66%
	Multi+3R	5.94	12.39	22.82	29.02%	-6.91%	-14.16%
#36	Uni	7.00	29.51	59.05	--	--	--
	Uni+3R	6.82	28.71	57.45	-2.54%	-2.71%	-2.71%
	Multi	8.12	24.61	50.10	16.11%	-16.60%	-15.16%
	Multi+3R	7.64	22.85	46.58	9.17%	-22.57%	-21.12%
		MX (×10⁶ kN·m)	*MY* (×10⁶ kN·m)	*MZ* (×10⁶ kN·m)	Δ*MX*	Δ*MY*	Δ*MZ*
#21	Uni	378.21	72.69	172.26	--	--	--
	Uni+3R	395.91	75.03	180.51	4.68%	3.23%	4.79%
	Multi	714.97	759.38	439.68	89.04%	944.73%	155.24%
	Multi+3R	701.42	756.73	433.79	85.46%	941.08%	151.82%
#36	Uni	840.89	170.52	378.70	--	--	--
	Uni+3R	818.11	166.15	368.11	-2.71%	-2.56%	-2.80%
	Multi	1019.83	869.14	405.08	21.28%	409.69%	6.97%
	Multi+3R	978.82	876.90	406.87	16.40%	414.24%	7.44%

rotational components affect the base reactions in a very mild way with the highest increase of 9.28% on *FX* under #21 and less than ±5% for the rest. The influence of non-uniformity is mainly reflected by the sharp rise of the peaks of overturning moment and torque. For event #21, *MY* increases 9.4 times and torque increases 1.5 times. For event #36, *MY* increases 4.1 times. This impact is enormous, which can bring high risk to the base of the structure. On the other hand, the axial force and shears for both events undergo much smaller but still obvious impact. *FX* increases 29.02% and 9.17% in Multi+3R for both events, while *FY* and *FZ* are substantially decreased.

The moment reactions are substantially affected by non-uniformity and multidimensionality of input, especially the overturning moment around the *Y* axis, which raises questions on the safety of the base. The flexural and torsional rigidities of the DICC need to

be checked or even strengthened when the seismic input is non-uniform and multidimensional. The huge discrepancy of *MY* due to multi-support input may be because some rocking modes of the DICC are excited by the non-uniformity of excitations. A similar study on the DICC also revealed an enormous rise of moment response due to multi-support input, even higher than that in this study (Zhao *et al*., 2016).

6.2 Local response

There is a total of 12168 nodes, 34819 beam elements and 3581 area elements in the DICC model. It is difficult to precisely locate the positions of the weak nodes or elements. Therefore, in local response analysis, two critical connection systems are used: the connecting bars between the main body and the roof, as well as the supporting columns of the curtain wall system (the elements highlighted in red in Fig. 3), which are selected as the research target.

6.2.1 Internal forces of connecting bars

The connecting bars are highlighted and labeled in Fig. 3(a). Figures 19 and 20 show the distribution of peak internal forces for events #21 and #36. The following features can be observed as follows. (1) Regardless of uniform input or non-uniform input, the rotational components hardly affect the internal forces in the bars. (2) The non-uniform input leads to some decrease in the reactions, especially under event #21 with the largest decrease of 38.5%. The situation for

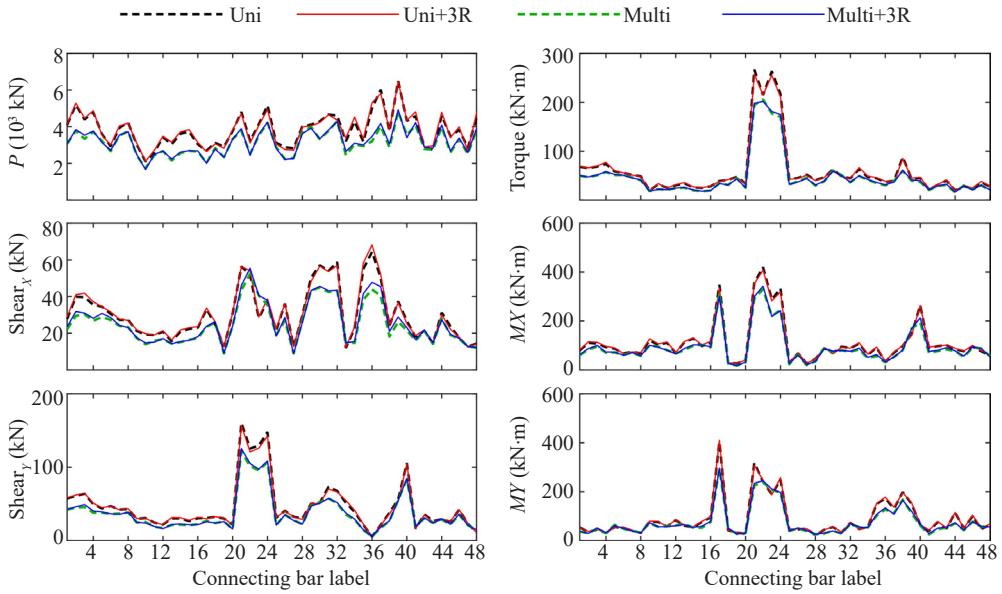

Fig. 19 Distributions of the peak internal forces of connecting bars for event #21

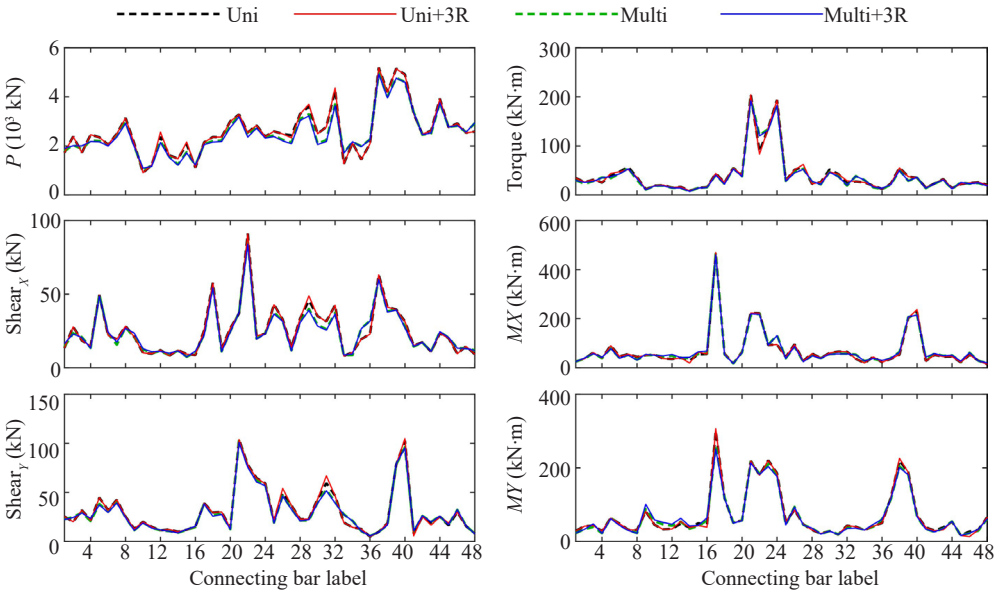

Fig. 20 Distributions of the peak internal forces of connecting bars for event #36

event #36 is different with negligible effects induced by the non-uniformity of input. (3) The non-uniformity and multidimensionality do not change the distribution mode of the internal forces, which is illustrated by the similarity of the peak lines.

6.2.2 Internal forces of support columns

The supporting columns are highlighted and labeled in Fig. 3(b). These columns mainly support the curtain wall system and the suspended part at the edge of the core tubes. Figures 21 and 22 show the distribution of peak internal forces for events #21 and #36. The following features can be observed. (1) The influence of the earthquakes shows large discrepancy with the greater increase in the column internal forces under event #21. The rotational components of event #21 have a considerable effect on the internal forces but have hardly any influence in event #36. (2) The impact can be divided into two groups: No. 1-16 columns undergo a decrease in internal forces while on the contrary, No.17-38 columns had a substantial rise in internal forces. This reveals that non-uniformity and multidimensionality of input can redistribute the loads from the inner part to the outer part, which suggests the members at the edge should be strengthened.

6.3 Discussion

Through the above analysis, the features of the seismic response of DICC under four loading cases are presented. Most of the findings are consistent with other research on this topic. Zhang *et al*. (2015) studied the dynamic response of the same DICC model

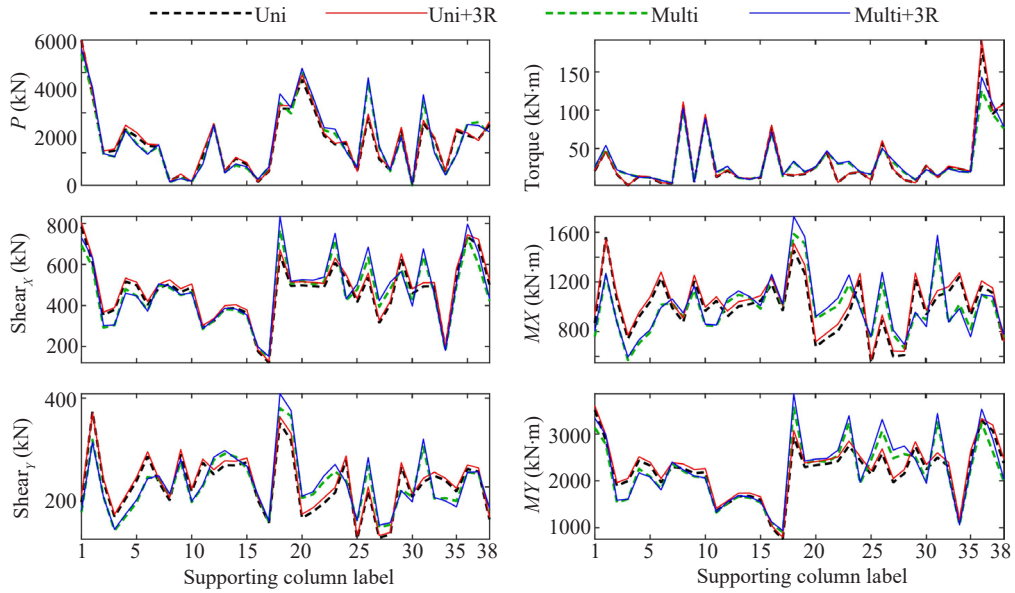

Fig. 21 Distributions of the peak internal forces of supporting columns for #21

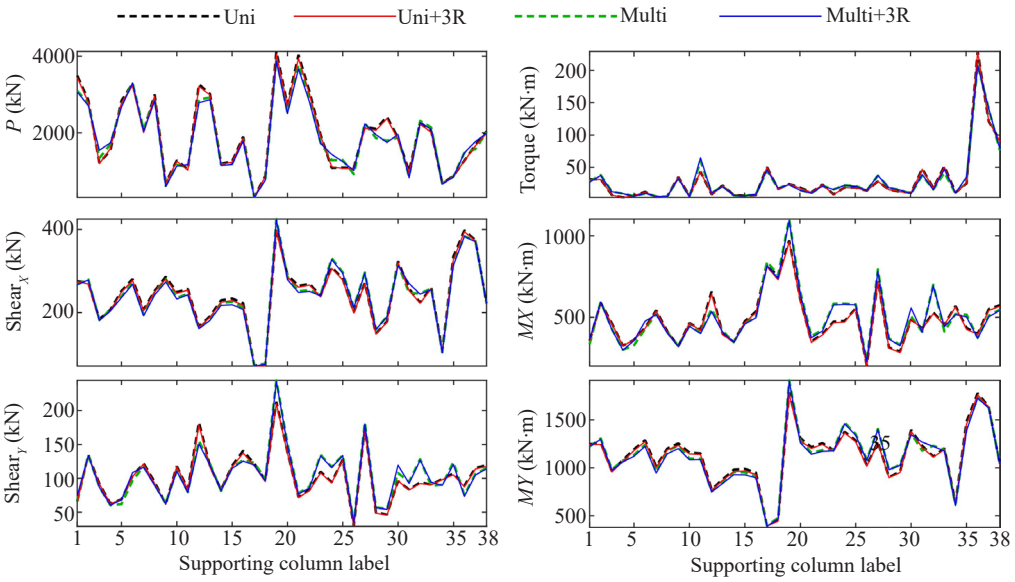

Fig. 22 Distributions of the peak internal forces of supporting columns for #36

under uniform translational and torsion seismic input and found that the torsion component increased the displacement response and the internal forces of the columns at the edge. Chen *et al*. (2014) conducted time history analysis on the cable supported barrel vault structure under multi-support seismic input and found that multi-support input can excite higher order modes which lead to the amplitude rise and uneven distribution of element internal forces. Zhang *et al*. (2019) analyzed the Jinan East Station, which is an irregular LSSS, under multi-support and multi-dimension earthquake excitation. It was found that multi-support and multi-dimension inputs increase the torsion response and reduce the shear reaction on the base. Lin *et al*. (2013) conducted shaking table experiments on a scaled long-span connected structure and confirmed the significant increase in overall response and diverse influence on element responses. Bai *et al*. (2010) proposed the time history analysis model for two typical types of LSSS subjected to spatial translational ground motions and drew similar conclusions.

Without consideration of specific details, the general trend of the findings in this study is mostly consistent with other researchers′ FE simulation and shaking table tests. The unique point of this study is that the influences on rotational directions (such as the point rotational angles and moments reactions) are higher than those on translational directions (such as the point translational displacements and force reactions). This may be explained by the introduction of three rotational ground motion components, which is hardly considered in other research.

With respect to the actuality and comprehensiveness of seismic excitation, the present research is novel and advanced, which is the reason for the inconsistencies between this study and previous research. Meanwhile, the multi-point and multidimensional input may make the results more reasonable and reliable.

7 Conclusion

This study investigates the seismic response of a LSSS (i.e., the DICC) under multi-support and multidimensional seismic excitations. The key findings include the following three points.

(1) Generally, the non-uniformity and multidimensionality of seismic input can increase the overall and local seismic responses of the LSSS. The commonly applied input model in seismic analysis, i.e., uniform translational motion input, may significantly underestimate the response of LSSSs, especially the base reactions.

(2) There is no obvious superposition effect between the influences from non-uniformity and multidimensionality of seismic inputs for the DICC. The response increase induced by non-uniformity is much higher than that induced by multidimensionality. The greatest influence induced by the multidimensionality is about 9.28% for the displacement and 9.50% for the internal force in the supporting columns. For non-uniformity, it is 88.26% for displacement and 9.4 times for the overturning moment at the base.

(3) The effects of non-uniformity and multidimensionality are strongly dependent on the input of the earthquake. As a typical distant earthquake, event #21 has a more significant influence than event #36, which is a typical near fault earthquake, in almost all the results. The difference in frequency content may be the major reason for this phenomenon. However, due to the limitation of the number of actual recordings from the dense array with a similar size of foundation, a more detailed analysis is required to better understand this observation.

References

Alexander NA (2008), "Multi-Support Excitation of Single Span Bridges, Using Real Seismic Ground Motion Recorded at the Smart-1 Array," *Computers & Structures*, **86**(1-2): 88–103.

Bai FL and Li HN (2010), "Seismic Analysis of Two Typical Spatial Structures Under Multi-Dimensional and Multi-Support Earthquake Excitations," *Journal of Dalian University of Technology*, **50**(6): 990–996. (in Chinese)

Chen Z, Zhao B, Wang Y and Shi Y (2014), "Seismic Response Analysis of Large-Span Cable Supported Barrel Vault to Multi-Support Excitations," *China Civil Engineering Journal*, **47**(S1): 59–64. (in Chinese)

GB 50011-2010 (2010), *Code for Seismic Design of Buildings*, China Archeitecture & Building Press, Beijing. (in Chinese)

GB 18306-2015 (2015), *Seismic Ground Motion Parameter Zonation Map of China*, Standardization Administration, Beijing. (in Chinese)

Gu ZY, Wang SG, Liu WQ, Du DS and Xu WZ(2017), "Experimental Research and Numerical Simulation of a Large-Span Isolated Structure Considering Multi-Dimensional Input Effects," *International Journal of Steel Structures*, **17**(4): 1583–1595.

Gupta VK and Trifunac MD (1990), "A Note on Contributions of Ground Torsion to Seismic Response of Symmetric Multistoried Buildings," *Earthquake Engineering and Engineering Vibration*, **10**(3): 27–40.

Gupta VK and Trifunac MD (1991), "Effects of Ground Rocking on Dynamic Response of Multistoried Buildings During Earthquakes," *Structural Engineering and Earthquake Engineering JSCE*, **8**(2): 43–50.

Imtiaz A, Perron V, Hollender F, Bard PY, Cornou C, Svay A and Theodoulidis N (2018), "Wavefield Characteristics and Spatial Incoherency: A Comparative Study from Argostoli Rock- and Soil-Site Dense Seismic Arrays," *Bulletin of the Seismological Society of America*, **108**(5A): 2839–2853.

Lee VW and Trifunac MD (1985), "Torsional Accelerograms," *International Journal of Soil Dynamics and Earthquake Engineering*, **4**(3): 132–139.

Lee VW and Trifunac MD (1987), "Rocking Strong Earthquake Accelerations," *Soil Dynamics and Earthquake Engineering*, **6**(2): 75–89.

Li C, Hao H, Li HN and Bi KM (2015), "Seismic Fragility Analysis of Reinforced Concrete Bridges with Chloride Induced Corrosion Subjected to Spatially Varying Ground Motions," *International Journal of Structural Stability and Dynamics*, **16**(1550010): 1–27.

Li C, Hao H, Li HN, Bi KM and Chen B (2017), "Modeling and Simulation of Spatially Correlated Ground Motions at Multiple Onshore and Seafloor Sites," *Journal of Earthquake Engineering*, **21**(3): 359–383.

Li C, Hao H, Li HN, Bi KM and Chen B (2018a), "Seismic Fragility Analyses of Sea-Crossing Cable-Stayed Bridges Subjected to Multi-Support Ground Motions on Offshore Sites," *Engineering Structures*, **165**(Jun.15): 441–456.

Li C, Li HN, Hao H and Bi KM (2018b), "Simulation of Spatially Varying Seafloor Motions Using Onshore Earthquake Recordings," *Journal of Engineering Mechanics*, **144**(9): 04018085.

Li C, Li HN, Hao H and Bi KM (2018c), "Simulation of Multi-Support Depth-Varying Earthquake Ground Motions Within Heterogeneous Onshore And Offshore Sites," *Earthquake Engineering and Engineering Vibration*, **17**(3): 475–490.

Li C, Li HN, Zhang, Su JS, Li RH and Ding YM (2020), "Seismic Performance Evaluation of Large-Span Offshore Cable-Stayed Bridges Under Non-Uniform Earthquake Excitations Including Strain Rate Effect," *Sci. China Technol. Sci*, https://doi.org/10.1007/s11431-020-1651-4.

Li HN, Wang SY and Wang QX (1997), "Response of Transmission Tower System to Horizontal and Rocking Earthquake Excitations," *Earthquake Engineering and Engineering Vibration*, **17**(4): 34–43.

Lin W, Chen SH, Yu JX and Qi A (2013), "Seismic Behavior of Long-Span Connected Structures Under Multi-Supported and Multi-Dimensional Earthquake Excitations," *Advances in Structural Engineering*, **16**(9): 1579–1586.

Luo C, Lou M and Gui G (2015), "Comparison for Calculation Methods of Long-Span Structure Under Multi-Support Seismic Excitation." *Journal of Tongji University* (*Natural Science*), **43**(1): 8–15. (in Chinese)

Mirzabozorg H, Akbari M and Hariri Ardebili MA (2012), "Wave Passage and Incoherency Effects on Seismic Response of High Arch Dams," *Earthquake Engineering and Engineering Vibration*, **11**(4): 567–578.

Mu Z, Yang Y, Chai L and Fan Z (2019), "Some Issues on Multi-Support Seismic Excitation of Ultra-Long Span Structure," *China Civil Engineering Journal*, **52**(11): 1–12. (in Chinese)

Quan W and Li H (2006), "State-of-the-Art Review on Multi-Component Multi-Support Seismic Response Analysis of Long-Span Structures," *Journal of Disaster Prevention and Mitigation Engineering*, **26**: 343–351. (in Chinese)

Soyluk K (2004), "Comparison of Random Vibration Methods for Multi-Support Seismic Excitation Analysis of Long-Span Bridges," *Engineering Structures*, **26**(11): 1573–1583.

Spudich P, Steck LK, Hellweg M, Fletcher J and Baker LM (1995), "Transient Stresses at Parkfield, California, Produced by the *M* 7.4 Landers Earthquake of June 28, 1992: Observations from the Upsar Dense Seismograph Array," *Journal of Geophysical Research*, **100**(B1): 675–690.

Tian L, Li HN and Liu GH (2010), "Seismic Response of Power Transmission Tower-Line System Subjected to Spatially Varying Ground Motions," *Mathematical Problems in Engineering*, 1–20.

Trifunac MD (2006), *Effects of Torsional and Rocking Excitations on the Response of Structures*, Earthquake Source Asymmetry, Structural Media and Rotation Effects, Berlin Heidelberg, Springer: 569–582.

Trifunac MD (2009), "Review: Rotations in Structural Response," *Bulletin of the Seismological Society of America*, **99**(2B): 968–979.

Wang L, Qu X, Ji D, Jiang B, Li F and An P (2012), "Structural Design and Research on Dalian International Conference Center," *Building Structure*, **42**(2): 1–6. (in Chinese)

Yadi S, Suhendro B, Priyosulistyo H, Aminullah A, Awaludin A, Matsumoto T, Pessiki S, Jonkers H, Siswosukarto S and Fajar Setiawan A(2019), "Dynamic Response of Long-Span Bridges Subjected to Nonuniform Excitation: A State-of-the-Art Review," *MATEC Web of Conferences*, 258.

Yang MF, Xu ZD, Huang XH and Ye HH (2014), "Analysis of the Collapse of Long-Span Reticulated Shell Structures Under Multi-Dimensional Seismic Excitations," *International Journal of Acoustics & Vibration*, **19**(1): 21–30.

Zhang G, Liu F, Yu Y, Song Z, Zhang Q, Ma M.and Wen K(2019), "Time-History Analysis of Jinan East Station Under Multi-Support and Multi-Dimension Seismic Excitation," *Building Science*, **35**(7): 114–118. (in Chinese)

Zhang J, Li HN and Wang L (2015), "The Research of Multi-Dimensional Seismic Responses of Large Span Asymmetric Spatial Structure," *Earthquake Engineering and Engineering Dynamics*, **35**(3): 1–9. (in Chinese)

Zhang J, Trifunac MD, Todorovska MI and Imtiaz A (2020a), *Estimating Rotations from Dense Arrays by Fitting a Surface to Earthquake Ground Displacements*

- *Part I: Data Preprocessing and Description of the Method*. (submitted for publication)

Zhang J, Trifunac MD, Todorovska MI and Imtiaz A (2020(b)), *Estimating Rotations from Dense Arrays by Fitting a Surface to Recorded Earthquake Ground Displacements - Part II: Analysis and Results*. (submitted for publication)

Zhao B, Wang Y, Chen Z, Shi Y, Jiang Y and Wang Y (2015), "Research on the Random Seismic Response Analysis for Multi- and Large-Span Structures to Multi-Support Excitations," *Earthquake Engineering and Engineering Vibration*, **14**(3): 527–538.

Zhao DH, Shen PJ and Liu GH (2016), "Dynamic Elastic-Plasticity Analysis of Long-Span Exhibition Hall Under Multi-Support Seismic Excitations," *Journal of Harbin Institude of Technology*, **48**(6): 70–74. (in Chinese)